PNAS RESEARCH ARTICLE | EARTH, ATMOSPHERIC, AND PLANETARY SCIENCES OPEN ACCESS

Global impacts of recent Southern Ocean cooling

Sarah M. Kang[a,b,1], Yue Yu[c], Clara Deser[d,1], Xiyue Zhang[e], In-Sik Kang[c], Sun-Seon Lee[f,g], Keith B. Rodgers[f,g], and Paulo Ceppi[h]

Contributed by Clara Deser; received January 16, 2023; accepted June 6, 2023; reviewed by Yue Dong and Masahiro Watanabe

Since the beginning of the satellite era, Southern Ocean sea surface temperatures (SSTs) have cooled, despite global warming. While observed Southern Ocean cooling has previously been reported to have minimal impact on the tropical Pacific, the efficiency of this teleconnection has recently shown to be mediated by subtropical cloud feedbacks that are highly model-dependent. Here, we conduct a coupled model intercomparison of paired ensemble simulations under historical radiative forcing: one with freely evolving SSTs and the other with Southern Ocean SST anomalies constrained to follow observations. We reveal a global impact of observed Southern Ocean cooling in the model with stronger (and more realistic) cloud feedbacks, including Antarctic sea–ice expansion, southeastern tropical Pacific cooling, northward-shifted Hadley circulation, Aleutian low weakening, and North Pacific warming. Our results therefore suggest that observed Southern Ocean SST decrease might have contributed to cooler conditions in the eastern tropical Pacific in recent decades.

Southern Ocean cooling | global teleconnection | tropical Pacific cooling | subtropical cloud feedback

Significance

In the recent past, the Southern Ocean has undergone a pronounced surface cooling; at the same time, the tropical Pacific has been cooling particularly in the eastern basin. However, these sea surface temperature (SST) trends are notoriously not captured by coupled global climate models under historical forcing. It is an open question if the missing Southern Ocean cooling signal partly explains the model-observation discrepancy in the recent tropical Pacific SST trends. A coupled model intercomparison study conducted here reveals a global teleconnection pattern driven by observed Southern Ocean SST decrease in the model with realistically strong cloud feedbacks. Our results thus suggest that Southern Ocean SST decrease is partly responsible for driving the southeastern tropical Pacific cooling in recent decades.

Despite the continued increase in greenhouse gases, surface cooling has been observed over the Southern Ocean since global satellite observations began in 1979 (1). A number of mechanisms have been proposed to account for the Southern Ocean cooling, including natural internal variability associated with deep ocean convection (2, 3), stratospheric ozone depletion (4), and Antarctic ice-sheet meltwater (5). The Southern Ocean cooling has also been suggested to be remotely driven by a La Niña-like cooling in the eastern tropical Pacific, with both linked to the negative phase of the Pacific Decadal Oscillation (6–8). Observed cooling in both the Southern Ocean and the tropical Pacific is notoriously not reproduced by climate models under historical forcing (9–11). The model-observation discrepancy may stem from numerous causes, for example, the dominance of internal variability in the observed trends, inadequate representation of the radiative forcing by the historical scenario in the CMIP protocol (12), and model deficiencies in representing important mechanisms such as tropical atmosphere-ocean coupling (13), Antarctic ice-sheet meltwater (5), cloud feedback (14), and stratospheric ozone depletion (15). This discrepancy in the historical period raises questions about the credibility of model projections for the coming decades. If the western Pacific continues to warm faster than the eastern Pacific, as it has in recent decades, then we can expect a stronger negative radiative feedback and lower transient climate sensitivity (16). Conversely, if the western Pacific warms less than the eastern Pacific, as most global circulation models project, then we expect a less negative feedback and a higher climate sensitivity (17). Hence, a better understanding of the origin of the model-observation discrepancy in the pattern of recent tropical warming remains an outstanding challenge with implications for future changes.

The hypothesis that the Southern Ocean cooling is linked to tropical variability (6, 7) aligns with the common notion that the tropics are effective drivers of extratropical climate anomalies via atmospheric Rossby waves (18). Meanwhile, more recent studies recognize the ability of the extratropics to influence the tropics through numerous pathways. For example, variability in Southern Ocean deep convection causes an interhemispheric energy imbalance, inducing cross-equatorial Hadley circulation changes and tropical rainfall shifts (19). Projected sea-ice loss in both the Arctic and Antarctic has an impact on the tropical Pacific sea surface temperature (SST) pattern, with enhanced warming in the eastern basin (20, 21). By contrast, aerosol-forced cooling in the northern extratropics induces enhanced cooling in the eastern equatorial Pacific (22, 23). A collapse of the Atlantic meridional overturning circulation causes a widespread cooling along the equatorial Pacific with an intensified Walker circulation (24). Southern Ocean heat uptake under global warming causes the Southeast Pacific to cool, thereby shifting the tropical precipitation northward (25). Finally, Antarctic meltwater-induced Southern Ocean cooling produces a pronounced cooling in the Southeast Pacific (5).

Author contributions: S.M.K., C.D., and I.-S.K. designed research; S.M.K. and Y.Y. performed research; S.M.K., Y.Y., X.Z., S.-S.L., K.B.R., and P.C. contributed new reagents/analytic tools; S.M.K. and Y.Y. analyzed data; and S.M.K. and C.D. wrote the paper.

Reviewers: Y.D., Columbia University; and M.W., Tokyo Daigaku - Kashiwa Campus.

The authors declare no competing interest.

[1]To whom correspondence may be addressed. Email: skang@unist.ac.kr or cdeser@ucar.edu.

This article contains supporting information online at https://www.pnas.org/lookup/suppl/doi:10.1073/pnas.2300881120/-/DCSupplemental.

Published July 17, 2023.

Based on a myriad of model-derived influences that support the capacity of extratropical perturbations to affect the tropical Pacific, one may suspect that recent observed Southern Ocean SST cooling is a viable candidate for contributing to the observed tropical Pacific cooling. This hypothesis has been evaluated in a recent study (1), where a minimal effect of observed Southern Ocean SST cooling on the tropical Pacific was found (albeit with a pronounced impact on the tropical Atlantic). It is critical to assess whether we can rule out the Southern Ocean contribution to the tropical Pacific cooling for elucidating the causes of the model-observation discrepancy in the historical climate change pattern. The result, however, is likely to be model dependent given the importance of subtropical low-cloud feedbacks in modulating teleconnections from the Southern Ocean (26). We are thereby motivated to address this matter with an intermodel assessment of the remote impact of observed Southern Ocean cooling, using models that differ in the degree of sophistication in representing subtropical low-cloud feedbacks.

Our intermodel comparison is built on the so-called Southern Ocean "Pacemaker" (SOPACE) simulation protocol in which a coupled model is forced by historical radiative forcing and its Southern Ocean SST anomalies are restored to the observed evolution from 1970 to 2014 (1) (*Materials and Methods*). We conduct a 21-member ensemble of SOPACE experiments with CESM2 (27) and compare it with the earlier CESM1 SOPACE ensemble conducted by ref. 1. The ERSSTv5 (28) observational product is used for CESM2 SOPACE as it is the latest generation with substantially more data than earlier versions, while ERSSTv3b (29) was used for CESM1 SOPACE. Differences between the two datasets in the Southern Ocean are taken into account in our intermodel comparison as described in *Materials and Methods*. The observed Southern Ocean SST cooling effect (denoted by SO-driven) is isolated by subtracting the ensemble-mean of the large-ensemble historical (HIST) simulations from the ensemble-mean of the SOPACE simulation of the same model (i.e., "SO-driven" =[SOPACE]−[HIST] where a squared bracket denotes the ensemble-mean). The CESM1 results are termed by an index "1" at the end of each experiment name (i.e., HIST1, SOPACE1, SO-driven1), and similarly for the CESM2 results (i.e., HIST2, SOPACE2, SO-driven2).

We find that the global teleconnection driven by the imposed transient cooling of Southern Ocean SSTs is highly model-dependent, with a stronger tropical Pacific response in CESM2 than CESM1 largely as a result of its stronger and more realistic subtropical stratocumulus cloud feedback (26, 30). However, it is important to note that the differences between SOPACE1 and SOPACE2 may stem not only from model structural uncertainty but also from forcing uncertainty due to the fact that the CESM1 experiments are conducted under the CMIP5 historical forcing protocol (31), whereas the CESM2 experiments follow the CMIP6 protocol (32). To quantify the forcing uncertainty, we also examine a new 10-member ensemble of CESM2 experiments under CMIP5 historical forcing (denoted as HIST2-C5). Assuming the climate response to observed Southern Ocean SST cooling is independent of radiative forcing, we infer the SOPACE response in this new CESM2-CMIP5 configuration by adding SO-driven2 to HIST2-C5, hereafter denoted SOPACE2-C5. We reveal substantial differences in the historical climate change pattern due to forcing uncertainties in CESM2: CMIP6 forcing induces a Northern Hemisphere warming and a northward displacement of the cross-equatorial Hadley circulation that are significantly stronger compared to CMIP5 forcing. While studies have examined how forcing uncertainties impact the global-mean surface temperature trend (12), this is the first study to quantify their effects on regional climate change patterns, demonstrating that the uncertainty arising from different forcings is comparable to or even larger than the uncertainty arising from different model versions.

Global Sea Surface Temperature Trends

We examine trends over the period 1979 to 2013 when significant surface cooling is observed over the Southern Ocean (Fig. 1*I* and *SI Appendix*, Figs. S1 and S2). The observed Southern Ocean cooling is absent in all ensemble members of HIST simulations, regardless of the forcing protocol (Fig. 1 *A*, *D*, and *G* and *SI Appendix*, Fig. S2). Enhanced equatorial Pacific warming in the radiatively forced response (Fig. 1 *A*, *D*, and *G*) is also inconsistent with the observed trend that instead shows a prominent cooling (Fig. 1*I*). The northern ocean basins exhibit a substantial warming in [HIST2] under CMIP6 historical forcing (Fig. 1*D*), while [HIST1] and [HIST2-C5] under CMIP5 forcing show only a modest warming (Fig. 1 *A* and *G*), highlighting both the model structural and forcing uncertainties. The contribution from the forcing uncertainty (i.e., [HIST2-C5] minus [HIST2]) is generally larger than the contribution from the model structural uncertainty (i.e., [HIST2-C5] minus [HIST1]) for the uncertainty in global SST trends (*SI Appendix*, Fig. S3).

The inconsistency between the model's forced response and observations may lead one to conclude that the observed Southern Ocean cooling is internally generated. However, it is also possible that the model-observation discrepancy arises from potential biases in the externally forced response and/or the lack of a dynamic Antarctic ice sheet model (33). The simulated impact of Antarctic meltwater has been shown to cause Southern Ocean cooling of comparable magnitude to observed trends in recent decades (*SI Appendix*, Fig. S4). While a quantitative estimation of Antarctic meltwater impacts is subject to large uncertainty, this leaves open the possibility that the observed Southern Ocean cooling is at least in part driven by external forcing, motivating us to conduct the SOPACE experiment.

In association with observed Southern Ocean cooling, [SOPACE] exhibits cooling extending into the Southeast Pacific (Fig. 1 *B*, *E*, and *H*), showing a better agreement with observed patterns (Fig. 1*I*) than the radiatively induced response (Fig. 1 *A*, *D*, and *G*). The SST trend pattern between 40°S and the equator is more strongly correlated with observations in [SOPACE] than in [HIST] for all model configurations (Fig. 1*J*). This suggests that the spatial pattern of observed SST trends over the entire Southern Hemisphere is substantially affected by observed cooling in a narrow meridional band over the Southern Ocean. The improvement for [SOPACE] compared to [HIST] is pronounced in both CESM2 configurations, with the pattern correlation enhanced from 0.01 to 0.51 under CMIP6 historical forcing and from 0.28 to 0.64 under CMIP5 historical forcing (Fig. 1*J*). The pattern correlation with observations lies within the range of pattern correlations between each ensemble member and the ensemble-mean for both [SOPACE2] and [SOPACE2-C5], but outside the range for [SOPACE1]. This indicates that the effect of Southern Ocean cooling is more extensive in CESM2, shaping the simulated SST trends over the entire Southern Hemisphere to be more realistic, relative to CESM1.

Indeed, the amplitude of SST trends over the Southeast Pacific (trapezoidal area indicated in Fig. 1*I*) exhibits large intermodel differences, especially in the SO-driven component (Fig. 1 *C*, *F*, and *K*). The Southeast Pacific cooling in SO-driven2 is 2.5 times stronger than that in SO-driven1 (−0.10 vs. −0.04 K/decade). As a result, none of the SOPACE1 ensemble members produce

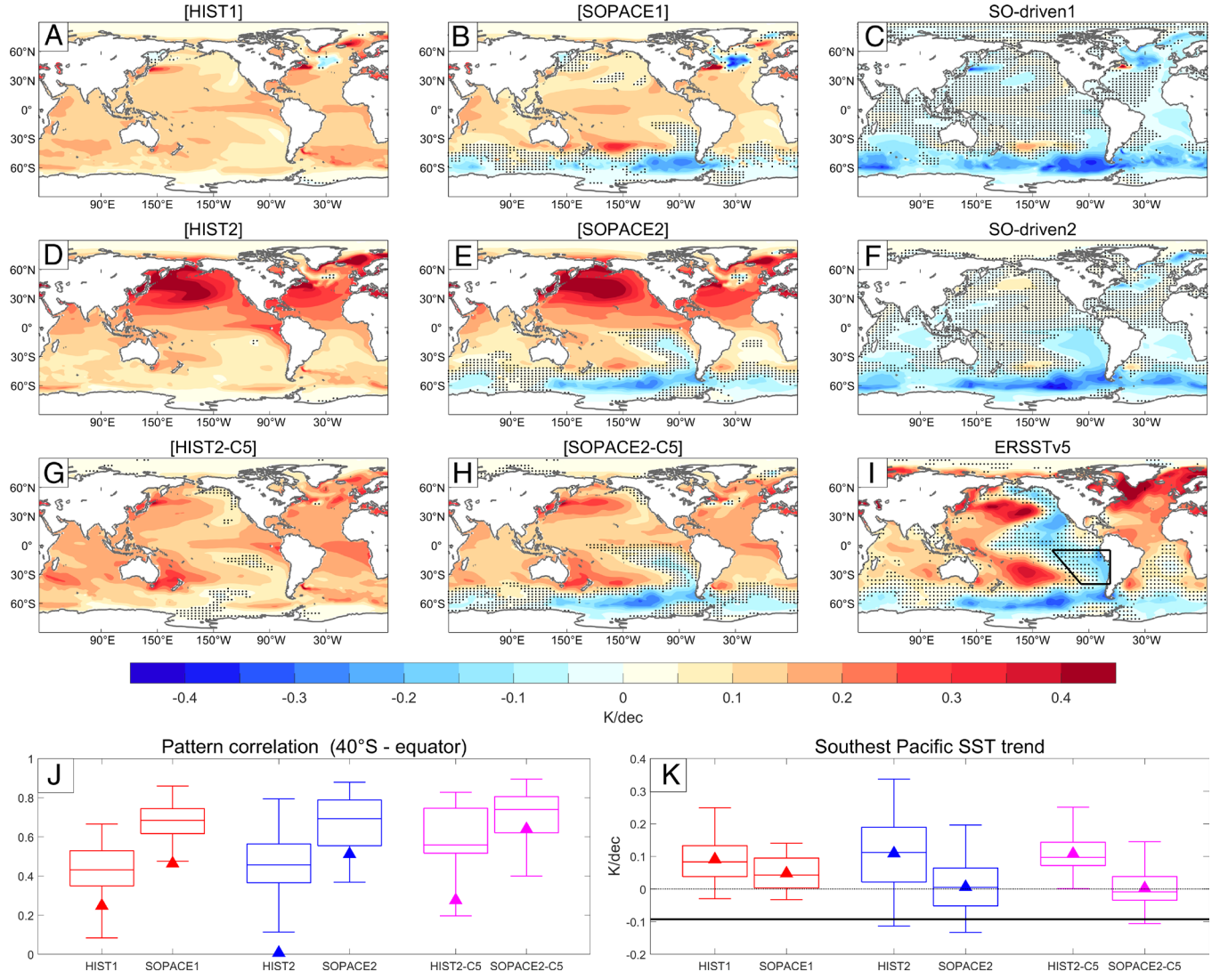

Fig. 1. Annual-mean SST trends between 1979 and 2013 in (*A*) [HIST1], (*B*) [SOPACE1], (*C*) SO-driven1, (*D*) [HIST2], (*E*) [SOPACE2], (*F*) SO-driven2, (*G*) [HIST2-C5], (*H*) [SOPACE2-C5], and (*I*) ERSSTv5. The trapezoidal region in (*I*) is used to denote the Southeast Pacific. Stippling indicates local trend that is not statistically significant at 95% confidence level. (*J*) Box-and-whisker plot of pattern correlations of SST trends in each ensemble member with those in the ensemble-mean between 40°S and the equator, with the box representing the first and third quartiles. Triangles show the pattern correlation between the ensemble-mean and the observation dataset, ERSSTv5. (*K*) Box-and-whisker plots of SST trends averaged over the Southeast Pacific (indicated in Fig. 1*I*). Triangles show the ensemble-mean values and black horizonal line shows the observed value.

cooling as large as with observations, whereas the bottom 25% of SOPACE2 ensemble members show Southeast Pacific cooling that is comparable to observations (Fig. 1*K*). That is, the Southern Ocean-driven Southeast Pacific cooling is sufficiently strong in CESM2 to offset the radiatively induced warming, in contrast to CESM1. However, it is important to note that the simulated Southeast Pacific cooling amplitude is subject to large uncertainty such that the ensemble spread is larger than the ensemble-mean difference between HIST and SOPACE, especially for CESM2. For the ensemble member of SOPACE2 that simulates the most realistic Southeast Pacific cooling trend (−0.10 K/decade compared to −0.09 K/decade in ERSSTv5), the Southern Ocean cooling effect (−0.10 K/decade; difference between the triangles in HIST2 and SOPACE2) and internal variability (−0.11 K/decade; difference between the triangle in SOPACE2 and the ensemble value of −0.10 K/decade) are equally important for counteracting the radiatively forced warming (0.11 K/decade; triangle in HIST2). This underscores the importance of conducting large ensembles to discern the impact of Southern Ocean cooling.

What are the processes that contribute to the intermodel difference in the remote Southeast Pacific response to Southern Ocean cooling? We address this question by examining the surface energy budget in SO-driven (26) (Fig. 2; *Materials and Methods*). In response to observed Southern Ocean cooling, the southeasterlies in the eastern basin of the South Pacific strengthen in conjunction with increased sea level pressure over southern high-latitudes, enhancing the evaporative cooling, thereby promoting equatorward propagation of a surface cooling response (Fig. 2 *G* and *H*). This wind-evaporation-SST (WES) feedback is likely to trigger cooling in the Southeast Pacific, which then stabilizes the atmospheric boundary layer aloft. The resultant increase in the lower tropospheric stability enhances subtropical low clouds that amplify the surface cooling via the shortwave radiative feedback (Fig. 2 *C* and *D* and *SI Appendix*, Fig. S5). Indeed, the shortwave radiative effect and the WES feedback are the dominant drivers of the Southeast Pacific cooling in both models (Fig. 2*K*). However, the contributions from the shortwave fluxes show a large intermodel difference: the shortwave flux (i.e., ΔT_{SW} in Fig. 2*K*)

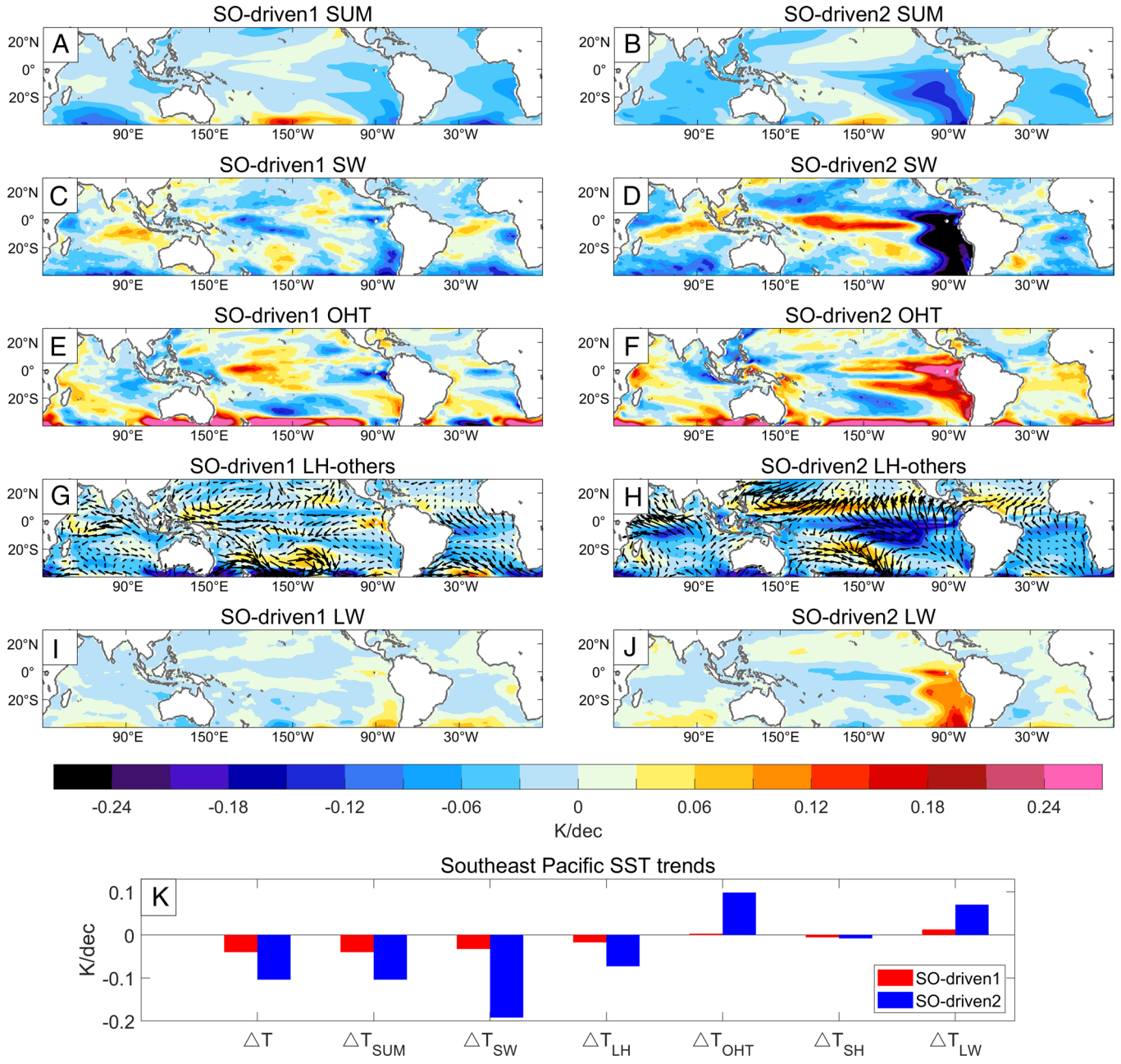

Fig. 2. SST trend decomposition via surface energy budget. (*A* and *B*) Net SST trends, and SST trends due to changes in (*C* and *D*) shortwave radiation, (*E* and *F*) ocean heat uptake, (*G* and *H*) latent heat fluxes due to wind speed changes, and (*I* and *J*) longwave radiation for (*Left*) SO-driven1 and (*Right*) SO-driven2. (*K*) SST trend decomposition averaged over the Southeast Pacific (region indicated in Fig. 1*I*).

in SO-driven2 is 6.3 times as large as that in SO-driven1. This is because in the Southeast Pacific, CESM2 features a strong shortwave low–cloud sensitivity to SST amounting to +2.23 W/m^2/K, close to the observed estimate of +2.21 W/m^2/K, as opposed to +0.66 W/m^2/K in CESM1 (*SI Appendix*, Figs. S6 and S7; *Materials and Methods*). The stronger shortwave-induced cooling response then leads to stronger southeasterly anomalies, further promoting the WES feedback (34). At the same time, more strongly intensified southeasterlies drive a larger southward Ekman heat advection, resulting in a larger negative feedback from the dynamic ocean contribution (35) in SO-driven2 compared to SO-driven1 (Fig. 2 *E*, *F*, and *K*). The negative feedback from the longwave component is also larger following the Planck and water vapor feedbacks (Fig. 2 *I*–*K*). However, larger negative feedbacks are overwhelmed by larger positive feedbacks, resulting in a more prominent cooling over the Southeast Pacific in SO-driven2 than SO-driven1 (Fig. 2 *A*, *B*, and *K*). In sum, the large intermodel difference in the remote response in SO-driven is because a teleconnection from the Southern Ocean to the Southeast Pacific is mediated by the highly model-dependent shortwave cloud feedback (26).

Global Circulation Changes

We further examine the global circulation trends during 1979 to 2013. Consistent with a weak interhemispheric contrast in surface temperature response under CMIP5 forcings (Fig. 1 *A* and *G*), the radiatively forced cross-equatorial Hadley circulation response is not statistically significant in [HIST1] and [HIST2-C5] (Fig. 3 *A* and *G*). In contrast, CMIP6 forcings cause an enhancement of

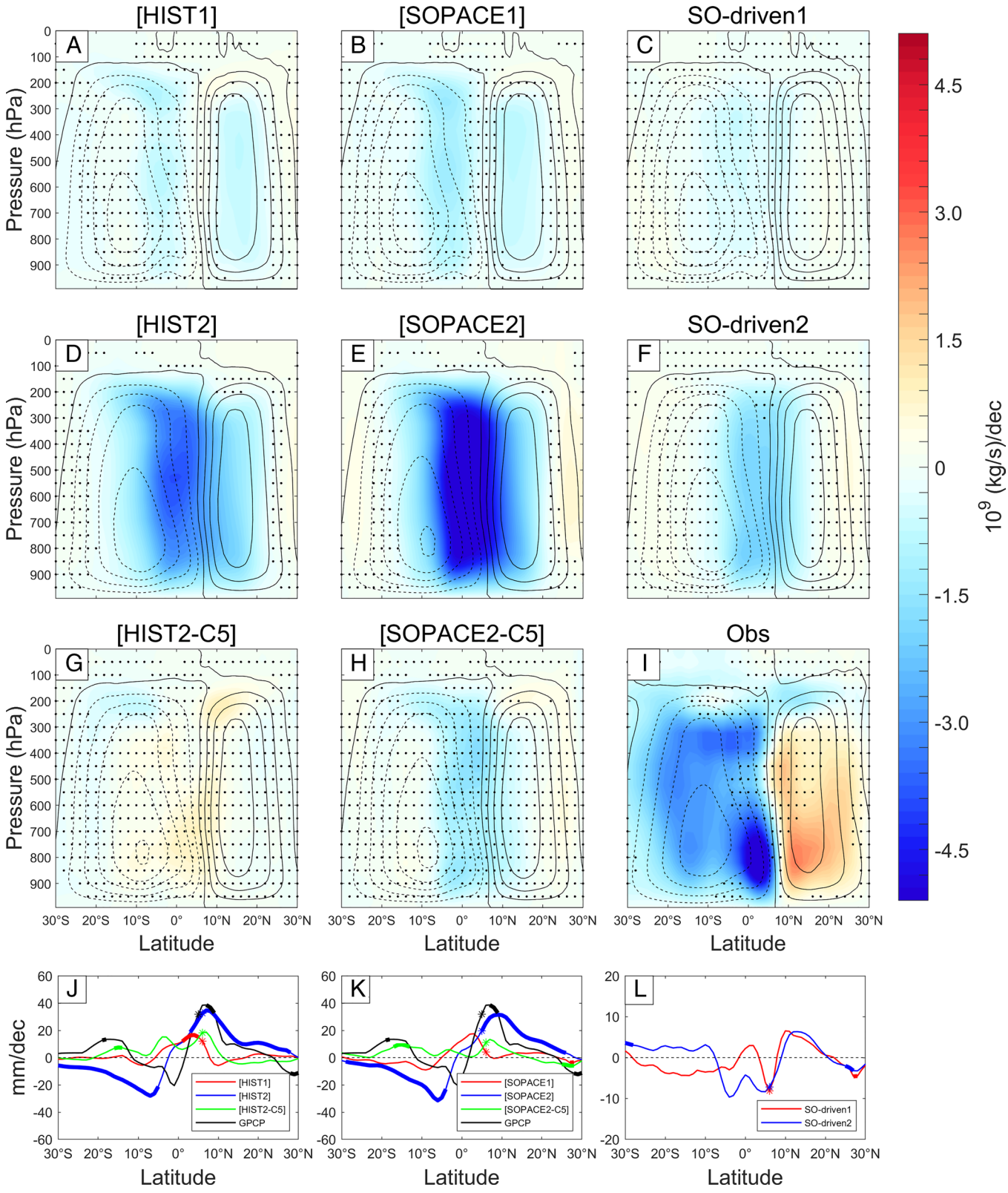

Fig. 3. Hadley circulation and tropical precipitation trends. Annual-mean mean meridional streamfunction trends in shading (positive: clockwise, negative: counter-clockwise) for (*A*) [HIST1], (*B*) [SOPACE1], (*C*) SO-driven1, (*D*) [HIST2], (*E*), [SOPACE2], (*F*) SO-driven2, (*G*) [HIST2-C5], (*H*) [SOPACE2-C5], and (*I*) ERA5 reanalysis (37), with the climatological mean in contours (solid: clockwise, dashed: counter-clockwise). Zonal-mean precipitation trends between 30°S and 30°N in (*J*) [HIST1] (red), [HIST2] (blue), and [HIST2-C5] (green), (*K*) [SOPACE1] (red), [SOPACE2] (blue), and [SOPACE2-C5] (green), and (*L*) SO-driven1 (red) and SO-driven2 (blue), with the observed estimate from GPCP data (38) in black lines in (*J* and *K*). Local trend that is not statistically significant at 95% confidence level is stippled in (*A*–*I*) and is plotted in thinner lines in (*J*–*L*).

the interhemispheric contrast in SST (Fig. 1*D*), giving rise to a northward displacement of the cross-equatorial Hadley circulation in [HIST2], as a way to restore the interhemispheric energy balance (36) (Fig. 3*D*). As a result, [HIST2] shows a clear northward shift of zonal-mean tropical precipitation, distinct from the highly equatorially symmetric response in [HIST1] and

[HIST2-C5] (Fig. 3*J*). Changes in the distribution of diabatic heating may feed back onto the Southeast Pacific SST cooling. The possible interplay between the tropical precipitation shift and the Southeast Pacific cooling is an important subject for future study. It is worth noting that the uncertainty in Hadley circulation and the associated zonal-mean tropical precipitation response arising from forcing uncertainty (Fig. 3*D* vs. Fig. 3*G*) dominates the uncertainty arising from model structural uncertainty (Fig. 3*A* vs. Fig. 3*G*), as highlighted in *SI Appendix*, Fig. S8.

In response to observed Southern Ocean SST decrease, the cross-equatorial Hadley circulation is displaced significantly northward in SO-driven2 (Fig. 3*F*) due to a prominent shortwave-induced cooling over the Southeast Pacific (Fig. 1*F*). Unlike with SO-driven2, the Hadley circulation anomaly is negligible in SO-driven1 (Fig. 3*C*), consistent with a limited Southern Ocean-driven teleconnection signal in the southeastern tropical Pacific SST (Fig. 1*C*). Consequently, the zonal-mean tropical precipitation clearly shifts northward in SO-driven2 whereas there is no clear shift in SO-driven1 (Fig. 3*L*). Nevertheless, the forcing uncertainty is still the dominant source of uncertainties in Hadley circulation response (*SI Appendix*, Fig. S8).

In particular, SO-driven2 shows a strong drying response across the equatorial Pacific in boreal winter/spring (*SI Appendix*, Fig. S9). As a consequence, the excitation of Rossby waves from the equatorial Pacific leads to a weakening of the Aleutian low in SO-driven2 (*SI Appendix*, Fig. S10*F*), particularly in boreal winter (though it is not statistically significant, *SI Appendix*, Fig. S11), resembling the teleconnection pattern during La Niña (39). Hence, the radiatively forced Aleutian low weakening, which emerges in all model configurations (*SI Appendix*, Fig. S10 *A*, *D*, and *G*), is amplified by the imposed Southern Ocean cooling in CESM2 but not in CESM1. As a result, the Aleutian low weakening becomes more prominent in [SOPACE2] but stays similar in [SOPACE1] (*SI Appendix*, Fig. S10 *B* and *E*) relative to their radiatively induced counterparts (*SI Appendix*, Fig. S10 *A* and *D*). Associated with an Aleutian low weakening in SO-driven2 is a significant warming of North Pacific SSTs (Fig. 1*F*), primarily due to enhanced downward shortwave fluxes and northward Ekman heat advection (*SI Appendix*, Fig. S12). As a result, the radiatively induced North Pacific warming in [HIST2] (Fig. 1*D*) is significantly amplified in [SOPACE2] (Fig. 1*E*), unlike the results for [HIST1] and [SOPACE1] (Fig. 1 *A* and *B*).

Antarctic Sea–Ice Trends

Despite global warming, Antarctic sea–ice expanded over 1979 to 2013 (40). The sea-ice expansion is observed over most of the Southern Ocean, with an exception over the West Antarctic coastline and north of the Weddell Sea due to warm-air advection associated with northerly wind anomalies (41) (Fig. 4*I*). As the observed Antarctic sea–ice increase has been partly attributed to the observed SST cooling and wind changes over the Southern Ocean (41, 42), here we examine if SOPACE can reproduce the observed Antarctic sea–ice trends. In stark contrast to the observed trends, the radiatively forced response shows sea-ice loss across all longitudes in all models (Fig. 4 *A*, *D*, and *G*). This radiatively forced sea-ice reduction is markedly offset by an Antarctic-wide sea-ice expansion in response to Southern Ocean cooling, which leads to an Antarctic-wide sea-ice expansion regardless of the model, as simulated in both SO-driven1 and SO-driven2 (Fig. 4 *C* and *F*). However, in general, Southern Ocean-induced sea-ice gain is more pronounced in SO-driven2 than in SO-driven1 (*SI Appendix*, Fig. S13*C*). To a large degree, this difference is due to slight differences in the spatial pattern of imposed SST anomalies in two different versions of observations (*SI Appendix*, Fig. S1; *Materials and Methods*). That is, the Southern Ocean region with a more (less) cooling in SOPACE2 compared to SOPACE1 exhibits a sea-ice expansion (reduction) in SO-driven2 relative to SO-driven1 (*SI Appendix*, Fig. S13*C*).

When combined with the radiatively induced response, [SOPACE2] shows a widespread increase in sea-ice, similar to observations, whereas [SOPACE1] shows positive sea-ice trends in the Bellingshausen Sea and negative trends in the Weddell Sea, the opposite to what is observed (Fig. 4 *B*, *E*, and *I*). As a result, [SOPACE2] shows a clear Antarctic sea–ice expansion, with an overall positive trend comparable to observations for the top 25% of the SOPACE2 ensemble, whereas [SOPACE1] shows a near-zero trend, with 60% of SOPACE1 ensemble members having negative trends that are opposite in sign to observations (Fig. 4*J*). As for the spatial correlation with observations, imposed Southern Ocean cooling leads to a considerable improvement in CESM2 (i.e., [SOPACE2] and [SOPACE2-C5]) from ~0 to 0.3, while the pattern correlation remains negative for [SOPACE1] (Fig. 4*K*). While the range of pattern correlations of each ensemble member with the ensemble-mean does not encompass the observed pattern correlation in all model experiments, it is worth noting that there is a considerable improvement when the SO-driven2 response is included. Our results suggest the importance of Southern Ocean SST evolution for reproducing the observed Antarctic sea–ice trends, as indicated by the fact that the differences between [SOPACE2] and [SOPACE1] sea–ice trends largely result from the differences in their Southern Ocean-driven responses (i.e., SO-driven2 minus SO-driven1) rather than the differences in their radiatively forced responses (i.e., [HIST2-C5]– [HIST2] and [HIST2-C5]– [HIST1]) (*SI Appendix*, Fig. S13).

Discussion

In this study, we identify a global teleconnection pattern driven by the observed Southern Ocean SST decreases in a coupled model that includes realistic subtropical shortwave cloud feedbacks (i.e., SOPACE2). This global response includes Antarctic sea–ice expansion, cooling of southeastern tropical Pacific and Atlantic SSTs, a northward shift of the Hadley circulation, drying of the equatorial Pacific, weakening of the Aleutian low, and warming of North Pacific SSTs. The tropical response to Southern Ocean SST cooling in CESM2 is largely confined to the southern hemisphere. This is in contrast to the effect of Southern Ocean radiative cooling, which induces a tropical response that penetrates into the northeastern Pacific (26) and leads to a strengthening of the Walker circulation (44). The origin of this difference in the efficacy of Southern Ocean cooling is left to future study. Nevertheless, our results provide compelling support for our mechanistic hypothesis whereby cooling of Southern Ocean SSTs over 1979 to 2013 is at least partly responsible for driving cooling of the southeastern tropical Pacific SSTs. The cooling of observed Southern Ocean SSTs may in turn have been internally generated (3), or externally forced via enhanced Antarctic meltwater (5, 33) and/or stratospheric ozone depletion (15), or some combination of internal and external factors. As this Southern Ocean-driven teleconnection is mediated by subtropical cloud feedbacks (26), this mechanistic pathway is largely indiscernible in the CMIP5-generation model that has unrealistically weak cloud feedbacks (1) (e.g., SO-driven1 vs. SO-driven2). Hence, correcting biases in cloud radiative feedback is a prerequisite for properly representing the remote teleconnection pattern.

Our results offer new insights into an outstanding discrepancy between models and observations in the pattern of recent tropical Pacific SST trends. According to our experiments, this discrepancy

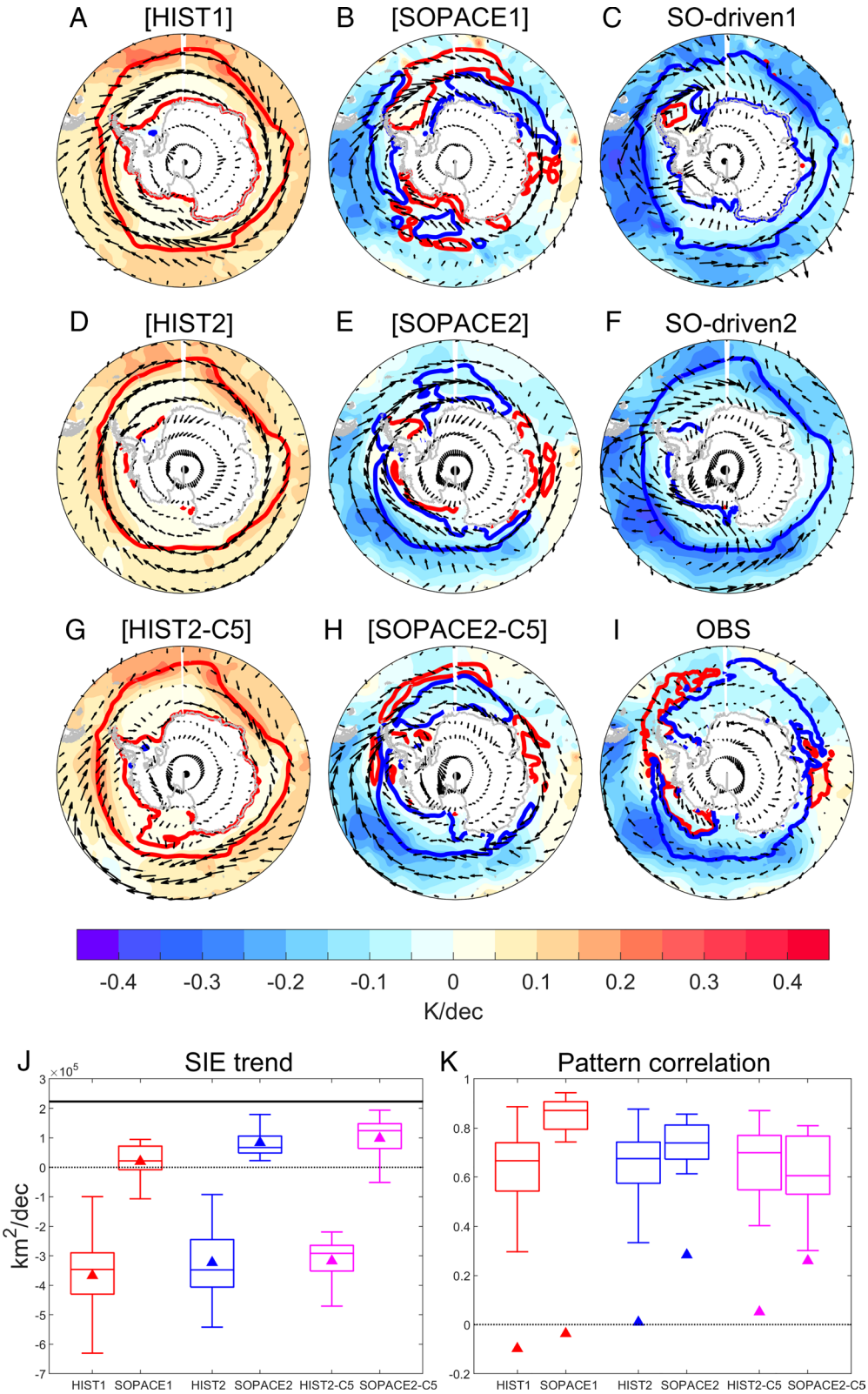

Fig. 4. Antarctic sea–ice extent and SST trends. Annual-mean trends between 1979 and 2013 of SST (shading), sea-ice extent (blue/red contours), and 1,000 hPa wind vectors in (*A*) [HIST1], (*B*) [SOPACE1], (*C*) SO-driven1, (*D*) [HIST2], (*E*) [SOPACE2], (*F*) SO-driven2, (*G*) [HIST2-C5], and (*h*), [SOPACE2-C5]. (*I*) Observed trends, with SST from ERSSTv5, sea-ice from the passive-microwave-derived NASA Goddard Bootstrap version 2 dataset (43), and winds from ERA5 reanalysis (37). Blue (red) contours outline regions with increasing (decreasing) sea-ice trend at 0.5 %/decade. (*J*) Box-whisker-plot of Antarctic sea–ice extent trends. Triangles show the ensemble-mean values and black horizonal line shows the observed value. (*K*) Box-and-whisker plot of pattern correlations of sea-ice trends in each ensemble member with those in the ensemble-mean between 50°S and 80°S. Triangles show the pattern correlation between the ensemble-mean and the observation.

might have resulted in part from the models' inability to reproduce the observed Southern Ocean SST decrease and the accompanying remote teleconnection pattern. In addition to the model structural uncertainty, we demonstrated that forcing uncertainty also contributes to the discrepancy (e.g., HIST2 vs. HIST2-C5), pointing to the need for more complete knowledge of historical radiative

forcings to improve the credibility of model simulations. In particular, forcing uncertainty dominates the model-dependence of trends in North Pacific and Atlantic SSTs (*SI Appendix*, Fig. S3) and the Hadley circulation (*SI Appendix*, Fig. S8). This is distinct from previously proposed mechanisms such as underestimation and/or phase mismatch of multidecadal variability in models relative to observations (6, 7, 45), a greenhouse gas–driven ocean thermostat effect (13, 46), and aerosol effects (23, 46).

As the Southern Ocean continues to absorb heat in the near future (47, 48), the Southern Ocean is projected to warm less than the rest of the global oceans. This relative SST cooling of the Southern Ocean will be reinforced by the cooling effect associated with the projected increase in Antarctic meltwater (5, 33). As a result, the near-future forced response of Southern Ocean SSTs is expected to induce global teleconnections similar to those found for recent decades according to our SOPACE experiments. By contrast, the rate of Southern Ocean SST warming is likely to increase rapidly on longer (century) timescales due to projected weakening of ocean heat uptake. Hence, whether the cooling trend observed over the Southern Ocean will be sustained into the future, for example due to increased Antarctic meltwater, or be reversed due to decreased ocean heat uptake, will determine the fate of Southern Ocean teleconnections to the eastern tropical Pacific. The sensitivity identified here with the CESM2 model suggests that the rate of eastern tropical Pacific SST warming will increase when Southern Ocean SSTs begin to warm, regardless of coupled model biases over the historical period (i.e., observed La Niña-like vs. simulated El Niño-like). This enhances our confidence in the future El Niño-like pattern of change projected by most climate models (49), whose time of emergence will depend in part on the balance between Southern Ocean anthropogenic heat uptake and Antarctic meltwater effects.

Materials and Methods

Model and Experiment Setup. We use the recently developed NCAR CESM2 with the Community Atmosphere Model version 6 (27) with nominal 1° horizontal resolution, which participated in the Coupled Model Intercomparison Project Phase 6 (CMIP6) (32). The radiatively forced component of CESM2 is obtained from the ensemble-mean of the first 50 members of the CESM2 Large Ensemble under CMIP6 historical radiative forcing (50) (HIST2). Note that biomass burning (BMB) emissions in this first 50-member set follow the CMIP6 protocol, whereas the second 50 members of the CESM2 Large Ensemble use an 11-y low-pass-filtered version of BMB emissions, which results in slightly less warming over the Northern Hemisphere (*SI Appendix*, Fig. S14). We then conduct a 21-member ensemble of the Southern Ocean Pacemaker (SOPACE2) experiment from 1970 to 2014 (1), which is similar to HIST2 except for restoring the SST anomalies at each grid box poleward of 40°S (with a linearly tapering buffer zone between 35°S and 40°S) to the observed evolution of SST anomalies taken from the National Oceanic and Atmospheric Administration (NOAA) ERSSTv5 dataset (28). In regions with HIST2 climatological sea-ice cover, SST is restored to the melting temperature of sea ice (−1.8 °C). The restoring time scale is 2 d for the model's 10-m deep ocean surface layer. We denote the ensemble-means of the HIST2 and SOPACE2 simulations with a bracket; these ensemble-means provide a good estimation of the radiatively forced response and the radiatively forced response plus the response to observed Southern Ocean SSTs, respectively. The difference between [SOPACE2] and [HIST2], which isolates the effects driven by the imposed Southern Ocean SST decrease, is termed SO-driven2. Our results from CESM2 are compared with those in ref. 1 from CESM1.1.2, which participated in CMIP5 (31). The corresponding CESM1.1.2 experiments are denoted as HIST1 (51), SOPACE1 (1), and SO-driven1.

Note that the observed SST dataset used to conduct SOPACE1 is ERSSTv3b (29), whereas ERSSTv5 is used for SOPACE2. While both datasets show a common Southern Ocean cooling trend for 1979 to 2013, there are nonnegligible differences in spatial pattern and amplitude, particularly in the high latitudes (*SI Appendix*, Fig. S1). In general, ERSSTv5 shows a greater cooling trend than ERSSTv3b. In the eastern Pacific sector (180°-70°W and 40°S-70°S), the Southern Ocean cooling trend in SO-driven2 is larger than that in SO-driven1 by a factor of 1.22. Because this region is particularly important for the Southern Ocean-to-tropics teleconnection (52), a factor of 1.22 is used to weight SO-driven1 for direct comparison to SO-driven2. Note that each ensemble member of SOPACE1 consists of 1) the radiatively forced component, [HIST1], 2) the internal variability, SOPACE1$_i$–[SOPACE1], where the subscript i denotes each ensemble member, and 3) the component driven by the imposed Southern Ocean SST decrease, w · SO-driven1, where w denotes the weighting factor of 1.22. The sum of (1)–(3), SOPACE1$_i$ – (1-w) · SO-driven1, defines the weighted SOPACE1. For the analysis, we use the weighted SOPACE1 and SO-driven1, to account for the difference in the imposed Southern Ocean cooling trends in SOPACE2 and SOPACE1 due to the use of different versions of ERSST.

Note that the weighting factor only corrects for the amplitude difference not the difference in spatial pattern. Differences in the spatial pattern of Southern Ocean SST trends in the two ERSST datasets are probably not important for the Southern Ocean–induced teleconnection pattern, but it appears to matter for regional differences in Antarctic sea–ice trends. The observed cooling trends over the Weddell Sea are greater in ERSSTv5 than ERSSTv3b, consistent with a larger sea-ice loss there in SO-driven2 relative to SO-driven1 (*SI Appendix*, Fig. S13*C*). Conversely, the observed SST cooling trend in the Bellingshausen Sea is weaker in ERSSTv5 than ERSSTv3b, consistent with a smaller sea-ice loss there in SO-driven2 relative to SO-driven1. Our results thus highlight the importance of reducing observational errors for attribution studies.

The SOPACE1 and SOPACE2 experiments are distinct not only in terms of their imposed Southern Ocean SST anomalies but also in their historical radiative forcings. The CESM2 experiments are forced by CMIP6 historical forcing while the CESM1.1.2 experiments are forced by CMIP5 historical forcing, obscuring the attribution of the differences between the two model results. Hence, we also examine a new 10-member ensemble of CESM2 simulations forced by CMIP5 historical forcing, denoted as HIST2-C5. We construct a synthetic version of SOPACE2 with HIST2-C5 (denoted as SOPACE2-C5) by adding SO-driven2 to each ensemble member of HIST2-C5.

SST Trend Decomposition via Surface Energy Budget. We use the same methodology as (1) to compute the surface energy budget and SST trend decomposition. The mixed layer energy budget states that:

$$\rho c_p H \frac{\partial T}{\partial t} = \mathrm{SW} + \mathrm{LW} - \mathrm{LH} - \mathrm{SH} + \mathrm{OHT}, \qquad [1]$$

where the left-hand-side represents the mixed-layer heat storage term, with ρ the density of ocean, c_p the specific heat of ocean, H the ocean mixed-layer depth, and T the mixed-layer temperature. The right-hand-side represents net downward surface energy, with SW net downward surface shortwave flux, LW net downward surface longwave flux, LH upward latent heat flux, SH upward sensible heat flux, and OHT ocean heat transport convergence. In order to isolate the forced response to imposed Southern Ocean SST trends, we compute the ensemble-mean trend of each term. As heat storage trends are negligible, OHT term can be computed as a residual term (i.e., net upward surface heat fluxes).

For a quasi-equilibrated state, Eq. **1** becomes

$$0 = \Delta\mathrm{SW} + \Delta\mathrm{LW} - \Delta\mathrm{LH} - \Delta\mathrm{SH} + \Delta\mathrm{OHT}, \qquad [2]$$

where Δ denotes the trend between 1979 and 2013. Following the strategy in ref. 25, we can rewrite Eq. **2** as a diagnostic equation of the SST trend. The bulk formula for evaporation states that latent heat flux changes related with Newtonian cooling can be expressed as $\Delta\mathrm{LH}_T = \alpha\overline{\mathrm{LH}}\Delta T$ where $\alpha \equiv \frac{L_v}{R_v\overline{T}^2}$, with the latent heat of vaporization L_v, the gas constant for moist air R_v, and overbars denoting the climatological mean. The remainder, $\Delta\mathrm{LH}_{others} \equiv \Delta\mathrm{LH} - \Delta\mathrm{LH}_T$, consists of latent heat flux changes due to changes in wind speed, changes in relative humidity, and changes in stability. Note that $\Delta\mathrm{LH}_{others}$ arises mainly through changes in wind speed. Then, we can rearrange Eq. **2** as

$$\Delta T = \frac{\Delta\mathrm{SW} + \Delta\mathrm{LW} - \Delta\mathrm{LH}_{others} - \Delta\mathrm{SH} + \Delta\mathrm{OHT}}{\alpha\overline{\mathrm{LH}}}, \qquad [3]$$

which decomposes the SST trends from SW, LW, wind-induced LH, SH, and ocean dynamics. Similarity between the sum of the five terms on the right-hand-side (ΔT_{net}) and the actual SST trend (ΔT) in Fig. 3*K* verifies the applicability of the decomposition.

Shortwave Low-Cloud Sensitivity to SST. We estimate shortwave low–cloud sensitivity to SST ($\partial C_{SW,low} / \partial SST$) in *SI Appendix*, Fig. S6 following the cloud-controlling factor analysis method (53). We only consider the radiative effect of low clouds (30). The cloud-controlling factor analysis framework assumes that low-cloud-induced shortwave radiative anomalies at each grid point r, $C_{SW,low}(r)$, is a function of local changes in six cloud-controlling factors: SST, estimated inversion strength (EIS), 700 hPa relative humidity (RH_{700}), 700 hPa vertical velocity (ω_{700}), horizontal advection of SST by the near-surface wind (SSTadv), and near-surface wind speed (WS):

$$dC_{SW,low}(r) \approx \frac{\partial C_{SW}(r)}{\partial SST(r)} dSST(r) + \frac{\partial C_{SW}(r)}{\partial EIS(r)} dEIS(r) + \frac{\partial C_{SW}(r)}{\partial RH_{700}(r)} dRH_{700}(r) + \frac{\partial C_{SW}(r)}{\partial \omega_{700}(r)} d\omega_{700}(r) + \frac{\partial C_{SW}(r)}{\partial SSTadv(r)} dSSTadv(r) + \frac{\partial C_{SW}(r)}{\partial WS(r)} dWS(r).$$

First, we calculate the monthly low-cloud-induced shortwave radiative anomalies, $dC_{SW,low}$. For observations, $dC_{SW,low}$ is calculated by convolving 20-y Moderate Resolution Imaging Spectroradiometer (MODIS) cloud fraction data from July 2002 to June 2022 (54), binned by cloud top pressure and optical depth, with a cloud-radiative kernel (55). We aggregate data from the lowermost two cloud top pressure bins in our calculation of $dC_{SW,low}$. For climate models, we proceed in the same way as for MODIS observations, but using historical monthly satellite simulator data for 1981 to 2000. All observational and model data are remapped onto a common 5° × 5° grid before further analysis.

Next, we calculate the cloud-radiative sensitivities, i.e., the partial derivatives $\partial C_{SW,low} / \partial X$ (where X denotes one of the six controlling factors), by ridge regression of $\partial C_{SW,low}$ onto the controlling factor anomalies ∂X at each grid point r (53). The monthly mean climatology for all variables is subtracted prior to analysis. For observations, the controlling factors are taken from monthly ERA5 reanalysis data (37). We define $\partial C_{SW,low} / \partial X$ with $X = SST$ as the shortwave low–cloud sensitivity to SST (*SI Appendix*, Fig. S6). The histogram of the Southeast Pacific average in 18 CMIP5/6 models is shown in *SI Appendix*, Fig. S7.

Data, Materials, and Software Availability. netcdf data have been deposited in Github (https://github.com/yuyuyaoyao/CESM2_SOPACE) (56).

ACKNOWLEDGMENTS. S.M.K. was supported by the Research Program for the carbon cycle between oceans, land, and atmosphere of the National Research Foundation (NRF) funded by the Ministry of Science and ICT (NRF-2022M3I6A1090965). NCAR is sponsored by the NSF. Y.Y. was supported by the Scientific Research Fund of the Second Institute of Oceanography, Ministry of Natural Resources (Grant No. JG2207) and the high-performance computing cluster of State Key Laboratory of Satellite Ocean Environment Dynamics. S.-S.L. and K.B.R. were supported by the Institute for Basic Science (IBS), Republic of Korea, under IBS-R028-D1. P.C. was supported by UK Natural Environment Research Council grants NE/T006250/1 and NE/V012045/1.

Author affiliations: [a]Department of Urban and Environmental Engineering, Ulsan National Institute of Science and Technology, Ulsan 44919, Republic of Korea; [b]Max Planck Institute for Meteorology, Hamburg 20146, Germany; [c]State Key Laboratory of Satellite Ocean Environment Dynamics, Second Institute of Oceanography, Ministry of Natural Resources, Hangzhou 310012, China; [d]Climate and Global Dynamics Laboratory, National Center for Atmospheric Research, Boulder, CO 80305; [e]Department of Earth and Planetary Sciences, Johns Hopkins University, Baltimore, MD 21218; [f]Center for Climate Physics, Institute for Basic Science, Busan 46241, Republic of Korea; [g]Pusan National University, Busan 46241, Republic of Korea; and [h]Department of Physics, Imperial College London, London SW7 2AZ, United Kingdom

1. X. Zhang, C. Deser, L. Sun, Is there a tropical response to recent observed southern ocean cooling? *Geophys. Res. Lett.* **48**, e2020GL091235 (2021).
2. M. Latif, T. Martin, W. Park, Southern ocean sector centennial climate variability and recent decadal trends. *J. Climate* **26**, 7767–7782 (2013).
3. L. Zhang, T. L. Delworth, W. Cooke, X. Yang, Natural variability of Southern Ocean convection as a driver of observed climate trends. *Nat. Climate Change* **9**, 59–65 (2019).
4. D. Ferreira, J. Marshall, C. M. Bitz, S. Solomon, A. Plumb, Antarctic ocean and sea ice response to ozone depletion: A two-time-scale problem. *J. Climate* **28**, 1206–1226 (2015).
5. B. Bronselaer *et al.*, Change in future climate due to Antarctic meltwater. *Nature* **564**, 53–58 (2018).
6. G. A. Meehl, J. M. Arblaster, C. M. Bitz, C. T. Y. Chung, H. Teng, Antarctic sea-ice expansion between 2000 and 2014 driven by tropical Pacific decadal climate variability. *Nat. Geosci.* **9**, 590–595 (2016).
7. E.-S. Chung *et al.*, Antarctic sea-ice expansion and Southern Ocean cooling linked to tropical variability. *Nat. Clim. Chang.* **12**, 461–468 (2022), 10.1038/s41558-022-01339-z (April 19, 2022).
8. D. P. Schneider, C. Deser, Tropically driven and externally forced patterns of Antarctic sea ice change: Reconciling observed and modeled trends. *Clim. Dyn.* **50**, 4599–4618 (2018).
9. M. Watanabe, J.-L. Dufresne, Y. Kosaka, T. Mauritsen, H. Tatebe, Enhanced warming constrained by past trends in equatorial Pacific sea surface temperature gradient. *Nat. Climate Change 11, 33–37* (2020), 10.1038/s41558-020-00933-3 (November 10, 2020).
10. S. Lee *et al.*, On the future zonal contrasts of equatorial Pacific climate: Perspectives from observations, simulations, and theories. *npj Clim. Atmos. Sci.* **5**, 82 (2022).
11. R. C. J. Wills, Y. Dong, C. Proistosecu, K. C. Armour, D. S. Battisti, Systematic climate model biases in the large-scale patterns of recent sea-surface temperature and sea-level pressure change. *Geophys. Res. Lett.* **49**, e2022GL100011 (2022).
12. J. C. Fyfe, V. V. Kharin, B. D. Santer, J. N. S. Cole, N. P. Gillett, Significant impact of forcing uncertainty in a large ensemble of climate model simulations. *Proc. Natl. Acad. Sci. U.S.A.* **118**, e2016549118 (2021).
13. R. Seager *et al.*, Strengthening tropical Pacific zonal sea surface temperature gradient consistent with rising greenhouse gases. *Nat. Climate Change* **9**, 517–522 (2019).
14. M. D. Zelinka *et al.*, Causes of higher climate sensitivity in CMIP6 models. *Geophys. Res. Lett.* **47**, e2019GL085782 (2020).
15. D. L. Hartmann, The Antarctic ozone hole and the pattern effect on climate sensitivity. *Proc. Natl. Acad. Sci. U.S.A.* **119**, e2207889119 (2022).
16. T. Andrews *et al.*, Accounting for changing temperature patterns increases historical estimates of climate sensitivity. *Geophys. Res. Lett.* **45**, 8490–8499 (2018).
17. Y. Dong, C. Proistosescu, K. C. Armour, D. S. Battisti, Attributing historical and future evolution of radiative feedbacks to regional warming patterns using a green's function approach: The preeminence of the Western Pacific. *J. Climate* **32**, 21 (2019).
18. B. J. Hoskins, D. J. Karoly, The steady linear response of a spherical atmosphere to thermal and orographic forcing. *J. Atmos. Sci.* **38**, 1179–1196 (1981).
19. A. Cabré, I. Marinov, A. Gnanadesikan, Global atmospheric teleconnections and multidecadal climate oscillations driven by southern ocean convection. *J. Climate* **30**, 8107–8126 (2017).
20. K. Wang, C. Deser, L. Sun, R. A. Tomas, Fast response of the tropics to an abrupt loss of arctic sea ice via ocean dynamics. *Geophys. Res. Lett.* **45**, 4264–4272 (2018).
21. M. R. England, L. M. Polvani, L. Sun, C. Deser, Tropical climate responses to projected Arctic and Antarctic sea-ice loss. *Nat. Geosci.* **13**, 275–281 (2020).
22. C. Deser *et al.*, Isolating the evolving contributions of anthropogenic aerosols and greenhouse gases: A new CESM1 large ensemble community resource. *J. Climate* **33**, 7835–7858 (2020).
23. S. M. Kang, S.-P. Xie, C. Deser, B. Xiang, Zonal mean and shift modes of historical climate response to evolving aerosol distribution. *Sci. Bull.* **66**, 2405–2411 (2021).
24. B. Oriheula-Pinto, M. H. England, A. S. Taschetto, Interbasin and interhemispheric impacts of a collapsed Atlantic Overturning Circulation. *Nat. Clim. Chang.* **12**, 558–565 (2022).
25. Y.-T. Hwang, S.-P. Xie, C. Deser, S. M. Kang, Connecting tropical climate change with Southern Ocean heat uptake. *Geophys. Res. Lett.* **44**, 9449–9457 (2017).
26. H. Kim, S. M. Kang, J. E. Kay, S.-P. Xie, Subtropical clouds key to Southern Ocean teleconnections to the tropical Pacific. *Proc. Natl. Acad. Sci. U.S.A.* **119**, e2200514119 (2022).
27. G. Danabasoglu *et al.*, The Community Earth System Model Version 2 (CESM2). *J. Adv. Model. Earth Syst.* **12**, e2019MS001916 (2020).
28. B. Huang *et al.*, Extended Reconstructed Sea Surface Temperature, Version 5 (ERSSTv5): Upgrades, validations, and intercomparisons. *J. Climate* **30**, 8179–8205 (2017).
29. T. M. Smith, R. W. Reynolds, T. C. Peterson, J. Lawrimore, Improvements to NOAA's Historical Merged Land-Ocean Surface Temperature Analysis (1880–2006). *J. Climate* **21**, 2283–2296 (2008).
30. T. A. Myers *et al.*, Observational constraints on low cloud feedback reduce uncertainty of climate sensitivity. *Nat. Clim. Chang.* **11**, 501–507 (2021).
31. K. E. Taylor, R. J. Stouffer, G. A. Meehl, An overview of CMIP5 and the experiment design. *Bull. Am. Meteorol. Soc.* **93**, 485–498 (2012).
32. V. Eyring *et al.*, Overview of the Coupled Model Intercomparison Project Phase 6 (CMIP6) experimental design and organization. *Geosci. Model Dev.* **9**, 1937–1958 (2016).
33. S. Sadai, A. Condron, R. DeConto, D. Pollard, Future climate response to Antarctic Ice Sheet melt caused by anthropogenic warming. *Sci. Adv.* **6**, eaaz1169 (2020).
34. W. Hsiao, Y. Hwang, Y. Chen, S. M. Kang, The role of clouds in shaping tropical pacific response pattern to extratropical thermal forcing. *Geophys. Res. Lett.* **49**, e2022GL098023 (2022).
35. S. M. Kang, Y. Shin, S.-P. Xie, Extratropical forcing and tropical rainfall distribution: Energetics framework and ocean Ekman advection. *Clim. Atmos. Sci.* **1**, 20172 (2018).
36. S. M. Kang, Extratropical influence on the tropical rainfall distribution. *Curr. Clim. Change Rep.* **6**, 24–36 (2020).
37. H. Hersbach *et al.*, Global reanalysis: Goodbye ERA-Interim, hello ERA5 (2019), 10.21957/VF291HEHD7 (September 27, 2022).
38. R. F. Adler *et al.*, The Version-2 Global Precipitation Climatology Project (GPCP) Monthly Precipitation Analysis (1979–Present). *J. Hydrometeorol.* **4**, 1147–1167 (2003).
39. K. E. Trenberth *et al.*, Progress during TOGA in understanding and modeling global teleconnections associated with tropical sea surface temperatures. *J. Geophys. Res. Oceans* **103**, 14291–14324 (1998).
40. C. L. Parkinson, A 40-y record reveals gradual Antarctic sea ice increases followed by decreases at rates far exceeding the rates seen in the Arctic. *Proc. Natl. Acad. Sci. U.S.A.* **116**, 14414–14423 (2019).

41. E. Blanchard-Wrigglesworth, L. A. Roach, A. Donohoe, Q. Ding, Impact of winds and southern ocean SSTs on Antarctic sea ice trends and variability. *J. Climate* **34**, 949–965 (2021).
42. T. Fan *et al.*, Recent Antarctic sea ice trends in the context of Southern Ocean surface climate variations since 1950. *Geophys. Res. Lett.* **41**, 2419–2426 (2014).
43. G. Peng, W. N. Meier, D. J. Scott, M. H. Savoie, A long-term and reproducible passive microwave sea ice concentration data record for climate studies and monitoring. *Earth System Sci. Data Discussions* **6**, 95–117 (2013).
44. S. M. Kang *et al.*, Walker circulation response to extratropical radiative forcing. *Sci. Adv.* **6**, eabd3021 (2020).
45. G. A. Meehl, H. Teng, J. M. Arblaster, Climate model simulations of the observed early-2000s hiatus of global warming. *Nat. Clim. Change* **4**, 898–902 (2014).
46. U. K. Heede, A. V. Fedorov, Eastern equatorial Pacific warming delayed by aerosols and thermostat response to CO2 increase. *Nat. Clim. Chang.* **11**, 693–703 (2021), 10.1038/s41558-021-01101-x (August 3, 2021).
47. J.-R. Shi, S.-P. Xie, L. D. Talley, Evolving relative importance of the southern ocean and north atlantic in anthropogenic ocean heat uptake. *J. Climate* **31**, 7459–7479 (2018).
48. K. C. Armour, J. Marshall, J. R. Scott, A. Donohoe, E. R. Newsom, Southern Ocean warming delayed by circumpolar upwelling and equatorward transport. *Nat. Geosci.* **9**, 549–554 (2016).
49. M. F. Stuecker, New insights into future tropical climate change. *Nat. Clim. Chang.* **11**, 645–646 (2021), 10.1038/s41558-021-01107-5 (August 3, 2021).
50. K. B. Rodgers *et al.*, Ubiquity of human-induced changes in climate variability. *Earth Syst. Dynm.* **12**, 1393–1411 (2021).
51. J. E. Kay *et al.*, The community earth system model (CESM) large ensemble project: A community resource for studying climate change in the presence of internal climate variability. *Bull. Am. Meteorol. Soc.* **96**, 1333–1349 (2015).
52. Y. Dong, K. C. Armour, D. S. Battisti, E. Blanchard-Wrigglesworth, Two-way teleconnections between the Southern Ocean and the tropical pacific via a dynamic feedback. *J. Climate* **35**, 2667–2682 (2022).
53. P. Ceppi, P. Nowack, Observational evidence that cloud feedback amplifies global warming. *Proc. Natl. Acad. Sci. U.S.A.* **118**, e2026290118 (2021).
54. R. Pincus *et al.*, Updated observations of clouds by MODIS for global model assessment (ESSD – Atmosphere/Atmospheric chemistry and physics, 2022), 10.5194/essd-2022-282. (April 17, 2023).
55. M. D. Zelinka, S. A. Klein, D. L. Hartmann, Computing and partitioning cloud feedbacks using cloud property histograms: Part I: Cloud radiative kernels. *J. Climate* **25**, 3715–3735 (2012).
56. Y. Yu, CESM2's SO pacemaker experiment output. *CESM2_SOPACE*. https://github.com/yuyuyaoyao/CESM2_SOPACE. Deposited 21 June 2023.